Journal of Materials Chemistry C

ROYAL SOCIETY OF CHEMISTRY

PAPER

View Article Online
View Journal | View Issue

Cite this: J. Mater. Chem. C, 2023, 11, 12570

The effect of inert dopant ions on spin-crossover materials is not simply controlled by chemical pressure†

Prabir Ghosh,[a] Christopher M. Pask,[b] Hari Babu Vasili,[c] Nobuto Yoshinari,[d] Takumi Konno,[d] ‡[d] Oscar Cespedes,[c] Cristian Enachescu,[e] Pradip Chakraborty *[f] and Malcolm A. Halcrow *[b]

$[Fe(bpp)_2][BF_4]_2$ (bpp = 2,6-*bis*{pyrazol-1-yl}pyridine) undergoes abrupt thermal spin-crossover (SCO) at 261 K with a small 2–3 K thermal hysteresis. Different compositions of doped materials $[Fe_zZn_{1-z}(bpp)_2][BF_4]_2$ and $[Fe_zRu_{1-z}(bpp)_2][BF_4]_2$ ($0 < z < 1$) show similar broadening of the SCO transition with increased doping, but differ in their effect on the transition temperature. Doping with zinc strongly lowers $T_{\frac{1}{2}}$, which is consistent with previous work. In contrast, doping with ruthenium increases $T_{\frac{1}{2}}$ to a smaller degree, which cannot be explained by the chemical pressure arguments that are conventionally applied to doped SCO materials. Mechanoelastic simulations imply that different dopants exert opposite effects on the lattice elastic interactions in the material during the SCO transition. Consistent with that, the materials show a complicated dependence of the crystallographic lattice parameters and thermal expansion properties on the iron spin state, for different dopant ions. These changes correlate with small perturbations to the molecular structure of high-spin $[Fe(bpp)_2]^{2+}$, in the presence of dopants with different geometric preferences and conformational rigidities. We conclude the effect of isomorphous dopants on $T_{\frac{1}{2}}$ reflects how the dopant influences the coordination geometry of the iron centres, as well as the chemical pressure exerted by the dopant ion size.

Received 28th July 2023,
Accepted 29th August 2023

DOI: 10.1039/d3tc02683c

rsc.li/materials-c

Introduction

Spin-crossover (SCO) materials undergo a spin state change under a physical or chemical stimulus.[1–5] The electronic rearrangement is accompanied by structural changes, which impact the colour,[6] volume,[7] conductivity,[8] permittivity[9] and other materials properties of a solid sample.[10–12] That switching functionality is being exploited in molecular electronics[8,13] and nanoscience,[5,14,15] while SCO materials are being investigated for solid state refrigeration,[16–19] mechanical actuation,[7,20–22] thermochromic printing[23,24] and other macroscopic applications.[6,25–28] Spin-transitions are also useful probes of crystal lattice dynamics, which allow the nucleation, growth and decay of new phases to be observed in real time.[29,30]

Most of these applications require materials undergoing first order spin-transitions, which arise from an interplay between the individual switching centres and the surrounding lattice.[31] Solid solutions of SCO compounds with inert isomorphous dopants have been essential for developing our understanding of that synergy. Early work on doped SCO materials showed how the strength and dimensionality of elastic interactions in a lattice controls the cooperativity of phase transformations,[32,33] leading to the development of Monte Carlo methods for simulating SCO processes.[34] More recently, doped SCO materials have shed light on the kinetics of spin state relaxation processes at low temperatures.[33,35,36]

Isomorphous M^{2+} dopant ions in an iron(II) SCO material $[Fe_zM_{1-z}L_n]^{m+}$ (M = Mn, Co, Ni, Zn *etc.*; L = a ligand) reduce the transition cooperativity as z decreases. That reflects the weakening of elastic interactions between the switching centres, as they become separated by dopant molecule spacers in the

[a] Department of Mechanical Engineering, Indian Institute of Technology Kharagpur, Kharagpur-721302, India
[b] School of Chemistry, University of Leeds, Woodhouse Lane, Leeds LS2 9JT, UK. E-mail: m.a.halcrow@leeds.ac.uk
[c] School of Physics and Astronomy, W. H. Bragg Building, University of Leeds, Leeds LS2 9JT, UK
[d] Department of Chemistry, Graduate School of Science, Osaka University, Toyonaka, Osaka 560-0043, Japan
[e] Faculty of Physics, Alexandru Ioan Cuza University, 700506 Iasi, Romania
[f] Department of Chemistry, Indian Institute of Technology Kharagpur, Kharagpur-721302, India. E-mail: pradipc@chem.iitkgp.ac.in

† Electronic supplementary information (ESI) available: X-ray powder diffraction and magnetic susceptibility data; crystallographic experimental data, refinement procedures, Figures and tabulated metric parameters; calculated thermal expansion coefficients from the compounds in this work, and selected literature materials. CCDC 2261786–2261796. For ESI and crystallographic data in CIF or other electronic format see DOI: https://doi.org/10.1039/d3tc02683c

‡ Current address: Department of Chemistry, Faculty of Science, National Taiwan Normal University, Taipei 11677, Taiwan.

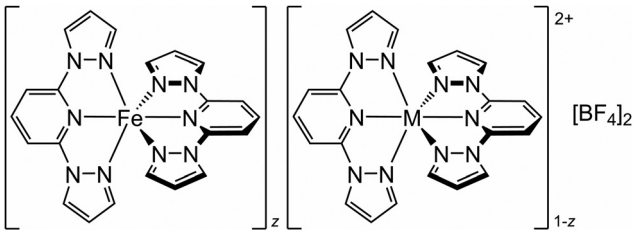

Scheme 1 The $[Fe_zM_{1-z}(bpp)_2][BF_4]_2$ materials referred to in this study (M^{2+} = Co^{2+}, Ni^{2+}, Zn^{2+} or Ru^{2+}; $0 < z < 1$).

lattice.[32–34] However, their effect on the transition temperature $T_{\frac{1}{2}}$ is more variable. While increased fractions of Mn^{2+}, Co^{2+} or Zn^{2+} dopant ions consistently lower $T_{\frac{1}{2}}$ of an iron(II) SCO compound,[32,36–51] Ni^{2+} dopants have a much smaller effect on $T_{\frac{1}{2}}$ of the same materials (Fig. S1, ESI†).[36,46–54] That is usually explained by the chemical pressure exerted by each dopant ion. The ionic radii of Mn^{2+} (83 pm), Co^{2+} (74.5 pm) and Zn^{2+} (74 pm) resemble high-spin Fe^{2+} (78 pm),[55] so introducing those dopant ions into the lattice should favour the high-spin state of the SCO material. In contrast, the ionic radius of Ni^{2+} (69 pm) is essentially the average of high-spin (78 pm) and low-spin (61 pm) Fe^{2+}, so doping an iron(II) lattice with Ni^{2+} has less effect on its internal chemical pressure.[32–34] By that argument, no dopant ion should increase $T_{\frac{1}{2}}$, since no common metal dications have ionic radii approaching low-spin Fe^{2+}.[56]

Chakraborty and co-workers recently reported that $[Fe_{0.65}Ru_{0.35}(ptz)_6][BF_4]_2$ (ptz = 1-propyltetrazole) exhibits $T_{\frac{1}{2}}$ = 135 K,[57] which is 10 K higher than for $[Fe(ptz)_6][BF_4]_2$ itself.[58] That was the first observation of chemical doping leading to stabilisation of the low-spin state of an SCO material. However, interpretation of that result is complicated by a crystallographic phase transition in $[Fe(ptz)_6][BF_4]_2$, which is associated with the SCO event and influences $T_{\frac{1}{2}}$, but is kinetically slow.[59–62] Other M^{2+} dopant ions in $[Fe_zM_{1-z}(ptz)_6][BF_4]_2$ affect $T_{\frac{1}{2}}$ and the phase transition temperature to different degrees, such that the two processes become decoupled at higher dopant levels.[63]

To clarify that observation, we have investigated the $[Fe_zM_{1-z}(bpp)_2][BF_4]_2$ system (Scheme 1; bpp = 2,6-*bis*{pyrazol-1-yl}pyridine). The parent complex $[Fe(bpp)_2][BF_4]_2$ undergoes an abrupt spin-transition at $T_{\frac{1}{2}}$ = 261 K with narrow thermal hysteresis, but without a crystallographic phase change.[64] Previous studies of $[Fe_zM_{1-z}(bpp)_2][BF_4]_2$ with M = Co^{2+} [42] or Ni^{2+} [54] showed typical trends for those dopants. Analogous materials with M = Zn^{2+} and Ru^{2+} are presented here, which confirm those dopant ions have opposing effects on $T_{\frac{1}{2}}$ in the $[Fe(bpp)_2][BF_4]_2$ lattice.[65] We show this reflects the geometric preferences and conformational flexibility of the different dopant ions, and how these perturb the local crystal lattice site structure.

Results

The starting materials $[M'(bpp)_2][BF_4]_2$ (M′ = Fe,[64] Zn[66] and Ru[67]) are crystallographically isomorphous. Co-crystallizing the iron complex with different mole ratios of the appropriate dopant from nitromethane, using diethyl ether vapour as the anti-solvent, yielded polycrystalline $[Fe_zZn_{1-z}(bpp)_2][BF_4]_2$ (**1a–1e**) and $[Fe_zRu_{1-z}(bpp)_2][BF_4]_2$ (**2a–2d**). Samples of **1a–1e** are yellow in colour which becomes paler as z decreases, while **2a–2d** become darker brown with increased ruthenium content.[68] The materials are phase-pure and isomorphous with the precursor complexes by powder diffraction (Fig. S2 and S3, ESI†). EDX analysis and magnetic measurements confirm the composition of each material is consistent with the stoichiometry of its crystallisation mixture (Table 1).

SCO in the new materials was monitored by magnetic susceptibility measurements (Fig. 1). The FeZn materials **1a–1e** show the expected trend, in that increasing zinc concentration leads to broadening of the transition, while significantly lowering $T_{\frac{1}{2}}$.[32,40,43–49] Ruthenium doping in **2a–2d** has a similar influence on the SCO cooperativity as the zinc dopant at each dopant concentration. However, the two dopant ions have opposite effects on the transition temperature, in that $T_{\frac{1}{2}}$ in **2a–2d** increases at higher ruthenium dopant levels (Fig. 1 and 2). The larger population of low-spin iron centres in the ruthenium-doped materials at room temperature is consistent with their brown colouration.[68]

Table 1 Analytical data for the new solid solution materials in this work. The stoichiometry z is the average of the three metal ion ratio calculations in the Table

					Fe:M calculated from:		
	z	C found (calcd)	H found (calcd)	N found (calcd)	Synthesis stoichiometry	EDX[a]	Magnetic data[b]
M = Zn							
1a	0.89	40.7(40.5)	2.73(2.78)	21.6(21.5)	0.89 : 0.11	0.90 : 0.10	0.89 : 0.11
1b	0.69	40.2(40.3)	2.68(2.77)	21.4(21.4)	0.68 : 0.32	0.70 : 0.30	0.69 : 0.31
1c	0.51	40.1(40.2)	2.69(2.76)	21.1(21.3)	0.50 : 0.50	0.55 : 0.45	0.49 : 0.51
1d	0.26	40.0(40.1)	2.82(2.75)	21.1(21.3)	0.28 : 0.72	0.24 : 0.76	0.27 : 0.73
1e	0.07	40.2(40.0)	2.87(2.75)	21.0(21.2)	0.08 : 0.92	0.06 : 0.94	0.07 : 0.93
M = Ru							
2a	0.88	39.9(40.2)	2.97(2.76)	20.9(21.3)	0.88 : 0.12	0.84 : 0.16	0.91 : 0.09
2b	0.67	39.4(39.6)	2.78(2.72)	20.7(21.0)	0.69 : 0.31	0.65 : 0.35	0.67 : 0.33
2c	0.49	38.9(39.2)	2.79(2.69)	20.4(20.8)	0.50 : 0.50	0.50 : 0.50	0.48 : 0.52
2d	0.14	38.0(38.3)	2.48(2.63)	19.9(20.3)	0.15 : 0.85	0.14 : 0.86	0.14 : 0.86

[a] Errors on the EDX data are between ±0.01–0.05 (Table S1). [b] Calculated assuming $\chi_M T$ = 3.5 cm^3 mol^{-1} K for high-spin Fe(II), and $\chi_M T$ = 0 for low-spin Fe(II) and the diamagnetic dopant ions. Estimated errors on these values are ±0.02.

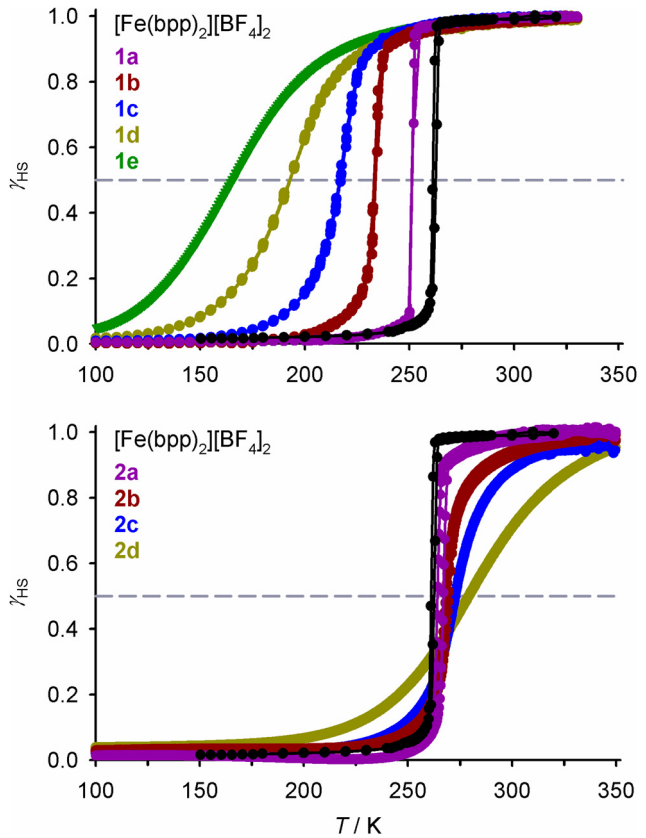

Fig. 1 Spin-crossover in $[Fe(bpp)_2][BF_4]_2$ and its solid solutions, from magnetic susceptibility data measured at a scan rate of 2 K min^{-1}. Data are plotted as the fraction of the sample that is high-spin at each temperature (γ_{HS}), and the transition midpoint at γ_{HS} = 0.5 is marked with a dashed line. Data points from each compound are linked by spline curves for clarity, Data for $[Fe(bpp)_2][BF_4]_2$ are taken from ref. 54.

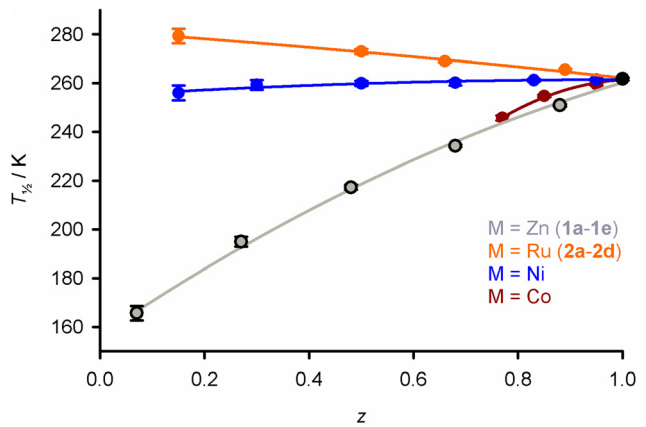

Fig. 2 Variation of $T_{\frac{1}{2}}$ with composition in $[Fe_zM_{1-z}(bpp)_2][BF_4]_2$ with different dopant ions, from magnetic susceptibility data measured at a 2 K min^{-1} scan rate (Fig. 1). Data for M = Ni and Co are taken from ref. 42 and 54.

These trends were confirmed by differential scanning calorimetry (DSC) measurements (Fig. S6 and S7, ESI†). The transition temperatures measured by DSC and the magnetic data

Table 2 SCO parameters for the materials in this work. ΔH and ΔS are quoted per mole of iron in the solid solutions. Estimated errors on $T_{\frac{1}{2}}$ from the DSC data are ±0.2 K

	Magnetic measurements		DSC		
	$T_{\frac{1}{2}}\downarrow$/K	$T_{\frac{1}{2}}\uparrow$/K	$T_{\frac{1}{2}}\uparrow$/K	ΔH/kJ mol^{-1}	ΔS/J mol^{-1} K^{-1}
$[Fe(bpp)_2][BF_4]_2$[a] M = Zn	261.0	262.5	263.2	21.8(2)	82.9(8)
1a	251.1	251.3	255.0	13.3(2)	52.2(8)
1b	233.6	233.2	237.7	6.6(4)	28(2)
1c	217.2	216.5	—[b]	—	—
1d	193	193	—[c]	—	—
1e	166	—	—[c]	—	—
M = Ru					
2a	264.1	265.0	269.1	18.6(2)	69.0(8)
2b	268.5	269.4	271.0	11.2(3)	41.3(11)
2c	272.7	272.7	274.6	8.4(7)	30(3)
2d	279	279	—[b]	—	—

[a] Taken from ref. 54. [b] DSC endotherms for **1c** and **2d** were too weak to be accurately measured. [c] Outside the temperature range of our calorimeter.

show minor differences, which we attribute to the different temperature ramps employed for the measurements (Table 2). However, the DSC data confirm $T_{\frac{1}{2}}$ in $[Fe_zM_{1-z}(bpp)_2][BF_4]_2$ decreases with z when M = Zn, but increases when M = Ru. ΔH and ΔS for the spin-transitions decrease more slowly with increased doping for M = Ru than for M = Zn at small dopant concentrations. DSC measurements at larger dopant levels were not achieved, because their endotherms were too weak or outside the temperature range of our calorimeter (T_{min} = 190 K).

The materials' SCO profiles were simulated using a 3D mechanoelastic approach.[69–71] The sample used is a lattice of 6400 molecules, represented as balls situated at the sites of a face-centered cubic structure of five interconnected layers with open boundary conditions (Fig. 3). All the bulk molecules have twelve nearest neighbours (six on the same layer and six on the adjacent layers), which are linked by springs.

The molecules can flip between spin states according to the Monte Carlo Arrhenius probabilities (eqn (1) and (2)):[34,72]

$$P^i_{HS\rightarrow LS} = \frac{1}{\tau}\exp\left(\frac{D - k_B T\ln g}{2k_B T}\right)\exp\left(-\frac{E_a - \kappa p_i}{k_B T}\right) \quad (1)$$

$$P^i_{LS\rightarrow HS} = \frac{1}{\tau}\exp\left(-\frac{D - k_B T\ln g}{2k_B T}\right)\exp\left(-\frac{E_a + \kappa p_i}{k_B T}\right) \quad (2)$$

where D and E_a are respectively the HS-LS energy difference and the transition activation energy for non-interacting molecules; g is the degeneracy ratio between the high- and low-spin states; T is the temperature; κ is a scaling factor between the local pressure and the activation energy; and τ is a scaling constant, chosen so the above probabilities are well below unity at any temperature. The key parameter in the above probabilities, responsible for the cooperativity in the system, is the local pressure force p_i, defined as the sum of elastic forces applied to

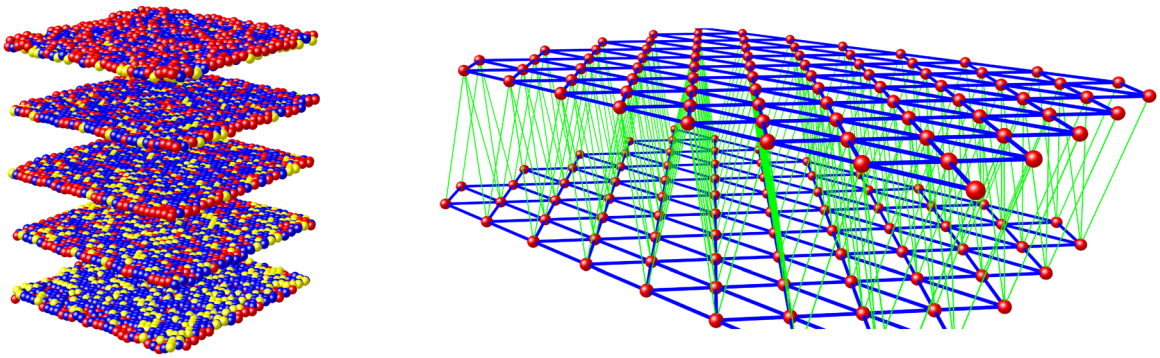

Fig. 3 Left: The simulation model comprising a five-layer fcc lattice containing high-spin (red), low-spin (blue) and dopant (yellow) molecule sites. Right: The links between molecules within and between the lattice layers (blue) and between two consecutive layers (green).

a molecule by all neighbouring springs (eqn (3)):

$$p_i = \sum_{\text{neighbour springs}} k\,\delta x_{ij} \qquad (3)$$

where δx_{ij} is positive for compressed springs and negative for elongated ones, and k is the elastic constant of the spring connecting each molecule pair. Thus, the switching probability is determined by the elongation of the springs: in the pure high-spin or low-spin states and in the absence of dopants, all the springs have their natural length. When a molecule flips, its size changes which elongates or compresses the neighbouring springs. Propagation of this perturbation induces all molecules in the system to change their absolute and relative positions.

During a Monte Carlo Step (MCS), all the molecules are checked to establish if they change state, by comparing the individual switching probability with a randomly generated number. After the completion of each MCS, the new equilibrium positions of the molecules are computed by solving differential equations considering the new molecular sizes. In this simulation we used a temperature sweep rate of 0.001 K per MCS, which is small enough to obtain a *quasi*-static thermal transition while minimizing kinetic effects. The radius of the molecules (including the ligand sphere) is 0.22 nm for HS and 0.20 nm for LS, with a distance of 1 nm between the centres of adjacent Fe ions.[32] The scaling factor κ takes the value 1450×10^{-14} J N^{-1}, similar to that in previous studies.[73]

First we determined which values of the elastic spring constant k give the best fit for the thermal transition loop from the pure iron compound, setting the experimental values for D and g ($g = \exp\{DS/k_B\}$). We found a value of $k = 5$ N m^{-1} within the layers in the lattice, which corresponds to a relatively high cooperativity, and ten times smaller between the layers. Recent experiments showed the stiffness of springs between molecules in different spin states can differ by 25–50%,[74] but this difference does not qualitatively change the simulation results.[75] Hence, to minimise the number of fitted parameters, we employed a single value of k between SCO molecules, irrespective of their state.

We introduced dopants into the system by randomly replacing fractions of SCO molecules with dopant molecules, represented as balls of a different radius. The radius of the zinc dopant molecules was set at 0.216 nm which is close to iron in its high-spin state, while the radius of the ruthenium dopant is 0.210 nm, the average of the two iron spin states in the model. Dopants are linked to neighbouring SCO molecules by different elastic constants, which depend on the state of the SCO molecules ($k = k_{DL}$ or $k = k_{DH}$ for springs linking dopants with low-spin and high-spin iron sites, respectively; Fig. 4). No other assumptions were made, and other parameters used to reproduce SCO in the pure iron compound were kept constant.

Fig. 4 presents simulations obtained with the following parameters: for Zn dopants, $k_{DL} = 6$ N m^{-1} and $k_{DH} = 4$ N m^{-1}; and for Ru dopants, $k_{DL} = 3$ N m^{-1} and $k_{DH} = 7$ N m^{-1}. This reproduces the shift of $T_{\frac{1}{2}}$ to lower temperatures for Zn doping and to higher temperatures for Ru doping, as observed experimentally. That is, the Zn(II) dopant ions in **1a–1e** and the Ru(II) dopants in **2a–2d** exert opposite influences on the lattice energetics of SCO in $[Fe(bpp)_2][BF_4]_2$.

Full crystallographic refinements were achieved from both spin states of **1c**, **2c** and $[Fe_{0.5}Ni_{0.5}(bpp)_2][BF_4]_2$ (**3c**),[54] using synchrotron radiation to maximize the resolution of the datasets. The structures were first refined as crystallographically ordered molecules, with mixed-composition metal atom sites.[36,40,41,45,76] The bond lengths and angles in the low-spin crystals, and in high-spin **1c**, are a good match for the weighted average values calculated from the two component molecules. However, the high-spin structures of **2c** and **3c** show some deviation from expectation (Table 3). Most notably, the *trans*-N{pyridyl}–M–N{pyridyl} angle (ϕ)[78] is larger than expected by 4–5σ, and is essentially equal to that of the ruthenium or nickel dopant molecule.[67,79]

The observed ϕ should be a weighted average of the iron and dopant molecule values (eqn (4)):[76]

$$\phi_{obs} = z\phi\{Fe\} + (1 - z)\phi\{M\} \qquad (4)$$

Eqn (4) estimates $\phi\{Fe, HS\} = 173.8(3)^\circ$ for high-spin **1c** at 300 K; $176.9(4)^\circ$ for **2c** at 350 K; and $176.2(3)^\circ$ for **3c** at 350 K. For comparison, $[Fe(bpp)_2][BF_4]_2$ exhibits $\phi\{Fe, HS\} = 173.15(10)^\circ$ at 290 K.[64] Hence, the high-spin $[Fe(bpp)_2]^{2+}$ centres in **1c** are unchanged by zinc doping within experimental error, but may adapt their geometries to the demands of the more rigid dopant molecules in **2c** and **3c**.[80] These small deviations

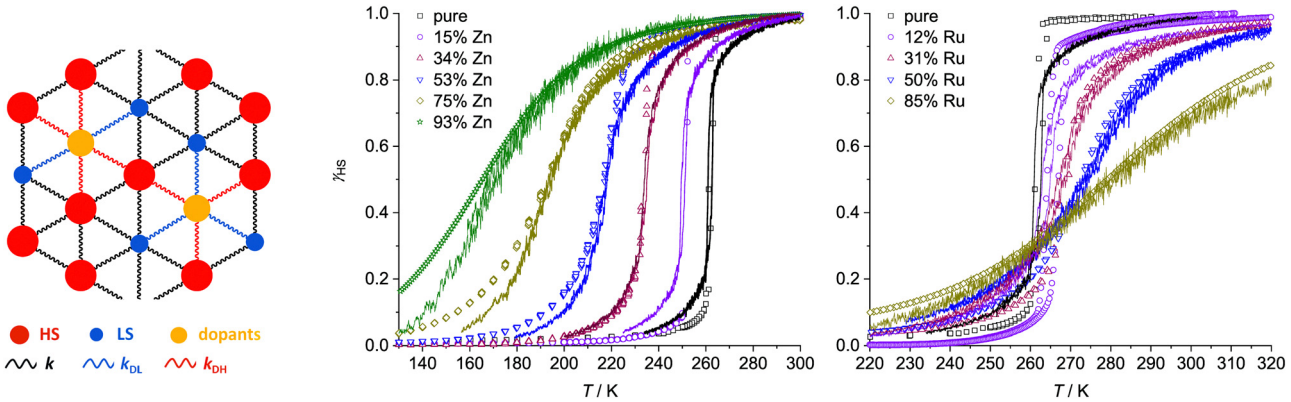

Fig. 4 Left: Schematic of an expanded layer of the simulation system showing dopants replacing SCO molecules, and their links with SCO nearest neighbours (HS = high-spin, LS = low-spin). The experimental (data points) and simulated (lines) thermal SCO transitions in **1a–1e** (centre) and **2a–2d** (right). The simulations show the equilibrated spin state population at each temperature for the *in silico* lattice in Fig. 3, using the dopant concentration and force constant parameters described in the text.[77]

Table 3 Summary structural data from the crystallographic refinements of **1c–3c**. The italicised values are weighted averages calculated from high-spin $[Fe(bpp)_2][BF_4]_2$ and the appropriate dopant complex, based on the metal compositions refined in the low temperature analyses (*cf.* eqn (4)). Complete lists of the bond lengths and angles are in Tables S3–S5 (ESI)[a]

	1c		**2c**		**3c**	
	HS, 300 K	LS, 100 K	HS, 350 K	LS, 100 K	HS, 350 K	LS, 100 K
M–N{pyridyl}$_{average}$	2.114(6) {*2.114(6)*}	1.996(2) {*1.993(4)*}	2.058(6) {*2.074(5)*}	1.950(3) {*1.962(4)*}	2.065(6) {*2.065{3}*}	1.959(2) {*1.962(3)*}
M–N{pyrazolyl}$_{average}$	2.184(10) {*2.183(10)*}	2.067(3) {*2.069(5)*}	2.119(12) {*2.137(8)*}	2.026(4) {*2.034(7)*}	2.143(13) {*2.144(6)*}	2.041(4) {*2.049(4)*}
γ/deg[b]	73.8(5) {*73.8(4)*}	77.19(14) {*77.4(3)*}	75.8(5) {*75.9(3)*}	79.03(17) {*79.2(3)*}	75.2(4) {*75.3(2)*}	78.38(14) {*78.37(18)*}
ϕ/deg[c]	173.8(2) {*173.5(2)*}	175.47(8) {*175.70(17)*}	177.6(3) {*175.7(2)*}	177.94(11) {*178.1(2)*}	176.6(3) {*175.20(12)*}	177.32(8) {*177.43(11)*}

[a] HS = high-spin, LS = low-spin. [b] γ is the average bpp ligand bite angle in the model, which is sensitive to the spin state and the composition of the metal content in the crystal. [c] ϕ is the *trans*-N{pyridyl}–M–N{pyridyl} bond angle.

will have little effect on the ligand field of the iron centres but should influence the lattice energy of the high-spin materials, thus changing the energetics of SCO.[81] This is discussed further below.

Whole molecule disorder models were constructed from the 100 K datasets of each crystal, to resolve their $[Fe(bpp)_2]^{2+}$ and $[M(bpp)_2]^{2+}$ (M = Zn, Ru or Ni) moieties. These refined without geometric restraints, although thermal parameter constraints were sometimes required between equivalent atoms in the two partial molecules. That allowed the metal composition of each crystal to be refined, which lay in the range $0.46 \leq z \leq 0.54$. The most precise disorder refinement is for **1c** (Fig. 5), because the geometry of its $[Zn(bpp)_2]^{2+}$ dopant is most different from the low-spin $[Fe(bpp)_2]^{2+}$ centres. Hence, those components are distinguished most clearly by the disorder model.

The geometries of $[Fe(bpp)_2]^{2+}$ and $[Zn(bpp)_2]^{2+}$ in **1c** are identical to the single-component crystals $[Fe(bpp)_2][BF_4]_2$ and $[Zn(bpp)_2][BF_4]_2$, within experimental error (Table S3, ESI†). The cation disorder refinements of **2c** and **3c** are less accurate and deviate slightly from expectation, particularly in their Fe–N{pyridyl} and M–N{pyridyl} bond lengths which are more

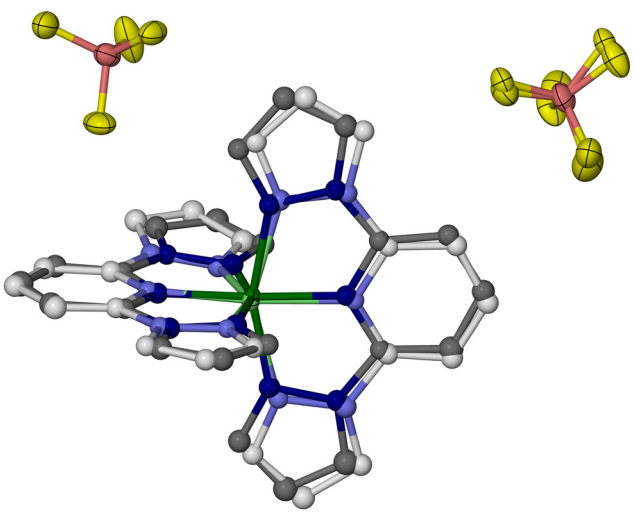

Fig. 5 The asymmetric unit of **1c** at 100 K showing the resolved $[Fe(bpp)_2]^{2+}$ (dark colouration) and $[Zn(bpp)_2]^{2+}$ (pale colouration) cation sites, which refined independently without restraints. Displacement ellipsoids are at the 50% probability level, and H atoms are omitted for clarity. Colour code: C, white or dark grey; B, pink; F, yellow; Fe, dark green; N, pale or dark blue; Zn, pale green.

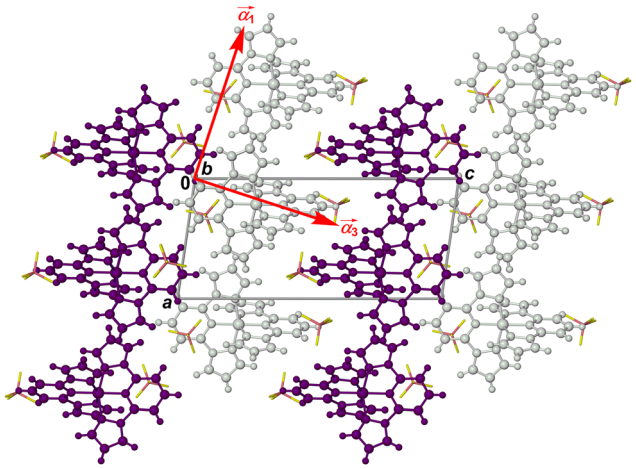

Fig. 6 Packing diagram of $[Fe(bpp)_2][BF_4]_2$ at 150 K,[64] viewed in the plane of the terpyridine embrace cation layers (Fig. S11, ESI†). Alternate cation layers are coloured white and purple, while the BF_4^- ions are de-emphasised for clarity. The red arrows show the approximate directions of the principal components of thermal expansion; the $\vec{\alpha_2}$ vector is oriented along *b*, perpendicular to the view.

similar than expected (Tables S4 and S5, ESI†). The resolution of the synchrotron diffraction data may be too low to fully define the disorder in that region of the asymmetric unit.

As previously described,[82] the crystals adopt a "terpyridine embrace" crystal lattice, which is often found in homoleptic complexes of 2,2′:6′,2″-terpyridine and related ligands.[83] The $[M(bpp)_2]^{2+}$ molecules associate into layers in the (001) crystal plane, through four-fold interdigitation of their distal pyrazolyl groups (Fig. 6 and Fig. S11, ESI†). Nearest neighbour cations within the layers are in close contact, through edge-to-face C–H···π and face-to-face π···π interactions between their pyrazolyl rings. Adjacent layers in the crystal are separated by the BF_4^- anions, and are not in direct van der Waals contact.

Unit cell data were collected at 10 K intervals between 350 and 100 K, from **1c–3c** and the precursor crystals $[M'(bpp)_2][BF_4]_2$ (M′ = Fe, Zn, Ni and Ru; Fig. 7). The isothermal volume change during the high → low-spin transition of the iron-containing crystals (ΔV_{SCO}) was calculated at $T_{\frac{1}{2}}$ (Table 4). The magnitude of ΔV_{SCO} shows significant variation, in the order **1c** < **2c** ≈ **3c** < $[Fe(bpp)_2][BF_4]_2$. ΔV_{SCO} for **2c** and **3c** is 54–62% that of the pure iron complex, reflecting that they contain *ca.* 50% of the iron content in the pure iron crystal.[76] Unexpectedly however, **1c** shows a much smaller ΔV_{SCO} which is *ca.* half that of the other solid solutions. This variation in ΔV_{SCO} has little effect on the SCO cooperativity in **1c**/**2c**/**3c**, which is very similar in each material from the magnetic susceptibility data (Fig. S21, ESI†).

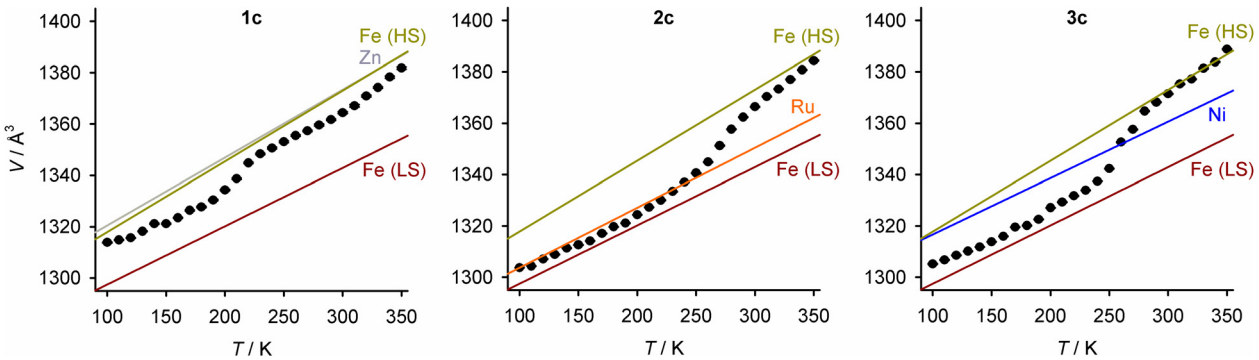

Fig. 7 Variable temperature unit cell volumes for **1c–3c**. Error bars are smaller than the symbols on the graphs. The lines show the thermal expansion linear regression fits for each $[M'(bpp)_2][BF_4]_2$ component in the crystal, as a pure material (HS = high-spin, LS = low-spin; Fig. S21–S22, ESI†).

Table 4 Absolute and % isothermal changes to the unit cell parameters during high → low-spin SCO in the iron-containing crystals, Δx_{SCO} (*x* = *a*, *b*, *c*, *β*, *V*). Data for each compound are calculated at $T_{\frac{1}{2}}$ (Table 2), by linear extrapolation of the low-spin and high-spin parameters to that temperature

		Δa_{SCO}/Å	Δb_{SCO}/Å	Δc_{SCO}/Å	$\Delta\beta_{SCO}$/deg	Δab_{SCO}[a]/Å	ΔV_{SCO}/Å^3
$[Fe(bpp)_2][BF_4]_2$	Δx_{SCO}	+0.0231(6)	+0.074(2)	−0.5570(9)	+2.027(5)	0.82(2)	−30.4(3)[b]
	%	+0.27	+0.87	−2.93	+2.11	+1.14	−2.23
1c	Δx_{SCO}	+0.0153(15)	+0.0428(11)	−0.222(3)	+0.666(13)	0.49(2)	−8.8(4)
	%	+0.18	+0.50	−1.18	+0.69	+0.68	−0.65
2c	Δx_{SCO}	−0.0093(7)	+0.0103(6)	−0.1993(16)	+0.724(8)	0.008(11)	−16.5(2)
	%	−0.11	+0.12	−1.06	+0.75	+0.01	−1.22
3c	Δx_{SCO}	−0.0041(8)	+0.0213(10)	−0.264(2)	+0.800(10)	0.146(16)	−18.8(3)
	%	−0.05	+0.25	−1.40	+0.83	+0.20	−1.38

[a] Δab_{SCO} denotes the change in the area of the 2D cation layers in the unit cell during SCO, where *ab* is the product of the *a* and *b* unit cell dimensions. [b] The isothermal ΔV_{SCO} for $[Fe(bpp)_2][BF_4]_2$ at 30 K has also been measured, at −29.3(5) Å^3 or 2.22%.[86]

The largest changes to the lattice during SCO involve the canting of the cation layers (the unit cell β angle), which is greater in the low-spin state; and, the spacing between them (the c dimension), which contracts in the low-spin material (Fig. 6). Both those changes contribute to the negative value of ΔV_{SCO}, as observed (Fig. 7 and Table 4). Those parameters behave quite consistently in **1c–3c**. Rather, the main differences between **1c–3c** during SCO lie in the dimensions of the cation layers in the ab plane. SCO in $[Fe(bpp)_2][BF_4]_2$ causes a small expansion of a and b in the low-spin state, despite the shorter distal Fe–N bond lengths in the low-spin molecule. That layer expansion is replicated in **1c**, roughly proportionately with its iron concentration. In contrast, the effect of SCO on a and b in **2c** and **3c** is much smaller. The expansion of the cation layers during SCO in **1c** partly offsets the other changes to the lattice, and is the main origin of its smaller ΔV_{SCO} volume contraction compared to **2c** and **3c**.

The area of the cation layers in all the single-component $[M'(bpp)_2][BF_4]_2$ lattices, as the product of a and b, shows a reasonable linear correlation with the bond angle ϕ (Fig. S23, ESI†). That is, the complex molecules pack less efficiently in two dimensions as ϕ approaches 180°, corresponding to idealised D_{2d} molecular symmetry. That explains the expansion of a and b in the low spin states of $[Fe(bpp)_2][BF_4]_2$ and **1c**. The change in ab during SCO at $T_{\frac{1}{2}}$ in the iron-containing compounds, Δab_{SCO}, decreases linearly with $\Delta\phi_{SCO}\{Fe\}$ for their iron centres, as estimated from eqn (4) (Fig. 8).

The unit cell data were used to calculate linear thermal expansion coefficients (α_V, eqn (5)).[84,85]

$$\alpha_V = \frac{1}{V_0}\left(\frac{dV}{dT}\right) \quad (5)$$

α_V is the inverse of the bulk modulus of a material, and is related to its compressibility; materials with a higher α_V are more susceptible to deformation. For consistency, the α_V values in Table 5 are scaled against the reference volume (V_0) at 100 K, which was derived by linear extrapolation of the experimental data if required. Although there is evidence of curvature in some of the V *vs.* T graphs (Fig. 7 and Fig. S21, S22, ESI†), the linear regression fits used to calculate $\alpha_V\{100\ K\}$ all gave $R^2 \geq 0.97$.

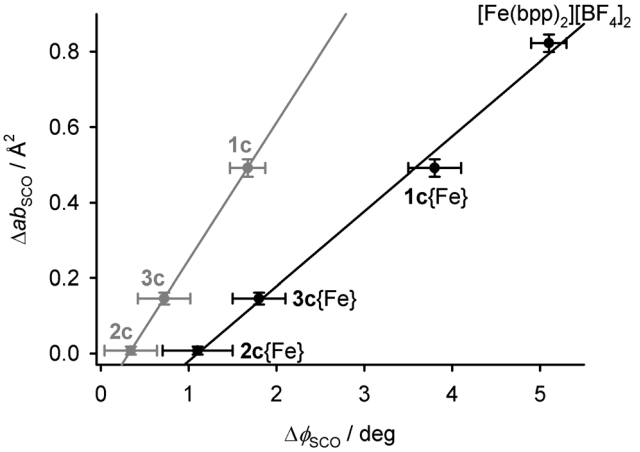

Fig. 8 The relationship between the changes in ϕ, and the area of the 2D cation layers, during SCO in the iron-containing crystals. The black datapoints are for the iron centres in **1c–3c**, calculated from eqn (4), while the grey points are directly measured values averaged between the iron and dopant complex molecules (Tables S2–S4, ESI†). Linear regression lines are included for both sets of data.

Table 5 Linear thermal expansion parameters for the compounds in this work, from single crystal unit cell data (Fig. S21 and S22, ESI). The values are scaled against the unit cell volume (V) at 100 K, which was derived by linear extrapolation of the experimental data if required[a]

	$\alpha_V\{100\ K\}$/ $10^6\ K^{-1}$	$\alpha_{TE}\{100\ K\}^b$/ $10^6\ K^{-1}$	$\alpha_3\{100\ K\}$/ $10^6\ K^{-1}$
$[Fe(bpp)_2][BF_4]_2$, HS	209(2)	38(3)	167.0(10)
$[Fe(bpp)_2][BF_4]_2$, LS	160(4)	82.0(15)	76(2)
1c, HS	213(8)	50(4)	158(4)
1c, LS	140(7)	57(3)	80(4)
2c, HS	273(2)	60(4)	208(6)
2c, LS	170(5)	90(2)	78(2)
3c, HS	251(8)	64(4)	182(4)
3c, LS	173(6)	88(3)	81(3)
$[Zn(bpp)_2][BF_4]_2$	204(7)	70(2)	127(5)
$[Ru(bpp)_2][BF_4]_2$	180(4)	66.3(16)	98(3)
$[Ni(bpp)_2][BF_4]_2$	168(4)	83.1(10)	93(3)

[a] HS = high-spin, LS = low-spin. [b] See eqn (6).

The $\alpha_V\{100\ K\}$ coefficients in Table 5 are typical for molecular crystals.[84,85] While they show some variation, $\alpha_V\{100\ K\}$ for the high-spin iron-containing materials is consistently larger than for their low-spin states.[76,87–89] The dopants $[Ni(bpp)_2][BF_4]_2$ and $[Ru(bpp)_2][BF_4]_2$ yield $\alpha_V\{100\ K\}$ values close to the low-spin iron crystals, whereas for $[Zn(bpp)_2][BF_4]_2$ it is nearer the high-spin iron range. $\alpha_V\{100\ K\}$ coefficients calculated using published unit cell data from other iron(II) SCO molecular materials and their zinc(II) analogs also conform to these trends (Table S14, ESI†). In particular, $\alpha_V\{100K\}$ for the zinc complexes is always 82–94% of the value for the isomorphous high-spin iron(II) complex.[89]

More insight is provided by the principal anisotropic components of the thermal expansion, which follow the same pattern in each crystal (Table S13, ESI†).[90] The two smallest component vectors (α_1 and α_2 in the Table) are oriented within the cation layers in the crystal. The largest component, α_3, the most deformable direction in the lattice, lies approximately perpendicular to the cation layers (Fig. 6). Since the intermolecular interactions in the lattice are weakest in that direction, these results are consistent with expectations.

The 2D thermal expansion coefficient of the terpyridine embrace cation layers, α_{TE}, is given by the sum in eqn (6).

$$\alpha_{TE} = \alpha_1 + \alpha_2 \quad (6)$$

Two trends are apparent when comparing the high-spin and low-spin forms of the iron-containing crystals (Table 5). First is that, for most of the crystals, $\alpha_{TE}[LS] > \alpha_{TE}[HS]$. The possible exception is **1c**, where the difference between α_{TE} in the two spin states lies within the experimental error. That trend in α_{TE}

does not reflect the deformability of the metal coordination sphere, which should be more rigid for low-spin iron(II).[80] Moreover, α_{TE} for the precursor crystals $[M'(bpp)_2][BF_4]_2$ also follows the trend M′ = Zn ≈ Ni < Ru. That is, the most conformationally rigid low-spin d^6 ruthenium(II) complex molecule forms crystals with the most deformable cation layers.

The second observation, exhibited by all the iron-containing crystals, is that $\alpha_3\{HS\} = 2–3 \times \alpha_3\{LS\}$. That is, high → low-spin SCO makes the crystal more deformable in the plane of the terpyridine embrace layers, but more rigid when deformed perpendicular to the cation layers. That is again mirrored in the $[M'(bpp)_2][BF_4]_2$ precursor crystals, where α_3 follows the trend M′ = Zn > Ni ≈ Ru. Thus, crystals of the largest and most flexible zinc(II) and high-spin iron(II) complexes are most susceptible to deformation between the cation layers. Of all these parameters, α_3 shows the most significant differences between the spin states, which is the origin of the consistent reduction in α_V during SCO.

Discussion

Derivatives of $[Fe(bpp)_2][BF_4]_2$ doped with inert metal ions, of formula $[Fe_zM_{1-z}(bpp)_2][BF_4]_2$, have now been produced with M = Co, Ni, Zn and Ru (Fig. 2). The first three dopant ions stabilise the high-spin state of the materials, in the expected order M = Co ≈ Zn > Ni for a given composition z (Fig. S1, ESI†).[32,33,48,49] In contrast, doping with Ru increases the transition temperature $T_{\frac{1}{2}}$, stabilising the low-spin state. Such trends have previously been explained by chemical pressure arguments, where larger dopant ions progressively stabilise the larger high-spin form of the iron centres.[32–34] While no ionic radius for Ru^{2+} is available,[55] the relative sizes of the dopant ions can be expressed by the octahedral coordination volume (V_{Oh}[91]) in their isomorphous $[M'(bpp)_2][BF_4]_2$ crystals. The trend in V_{Oh} runs as follows:

$$M' = Fe\{HS\}\ [12.378(9)\ Å^3] > Zn\ [12.251(12)] > Co\ [12.012(6)]$$

$$> Ni\ [11.320(5)] \approx Ru\ [11.279(10)] \gg Fe\{LS\}\ [9.620(5)]$$

On that basis, precedent predicts that $[Fe_zM_{1-z}(bpp)_2][BF_4]_2$ should behave similarly when M = Ni and Ru, as they do when M = Zn and Co (Fig. 2). Hence, the stabilisation of the low-spin state in $[Fe(bpp)_2][BF_4]_2$ by doping with ruthenium(II) cannot be rationalised from chemical pressure considerations.

Mechanoelastic simulations of the SCO curves show these trends can be explained, if the $[Zn(bpp)_2]^{2+}$ dopant molecules in **1a–1e** and the $[Ru(bpp)_2]^{2+}$ dopant in **2a–2d** exert opposite influences on the energetics of the $[Fe_zM_{1-z}(bpp)_2][BF_4]_2$ lattice. That is, intermolecular elastic interactions are stronger in the low-spin state of **1a–1e**, and in the high-spin state of **2a–2d** (Fig. 4). This is supported by a crystallographic comparison of $[Fe_zM_{1-z}(bpp)_2][BF_4]_2$ ($z \approx 0.5$; M = Zn, **1c**; M = Ru, **2c**; M = Ni, **3c**), which implies those three dopant ions affect the iron lattice in different ways. That is clear in their lattice properties, where the isothermal volume change during SCO (ΔV_{SCO}) in **1c** is only *ca* half the value for **2c** and **3c**. The difference mostly reflects the low-spin unit cell of **1c**, whose volume is significantly larger than for the other two materials (Fig. 7).

These changes in ΔV_{SCO} are anisotropic in nature (Table 4), so they do not simply originate from the different ionic radii of the dopant metal ions. Rather, they reflect the dimensions of the cation layers, which become measurably larger during SCO in **1c** but are almost unchanged in **2c** and **3c** (Table 4). This in turn correlates with the molecular structure changes during SCO at the iron sites in **1c–3c** (Fig. 8).

Related observations can be made from the thermal expansion coefficients of each material. All the iron-containing crystals are less deformable in their low-spin states (smaller α_V, Table 5), which reflects significant changes perpendicular to the cation layers during SCO. The cation layers themselves show the opposite trend, in being more deformable in the low-spin crystals than in their high-spin state (larger α_{TE}). However that trend is less pronounced in **1c** than in the other iron-containing crystals, where α_{TE} in both spin states lies within experimental error. That is more evidence that the lattice properties of **1c** are different from **2c** and **3c**.

At the molecular level, the crystallographic metric parameters in high-spin **2c** and **3c** deviate slightly from expectation, when considered as an average of their component molecules. This is most obvious in the ϕ angle, which is larger than predicted for high-spin **2c** and **3c** based on the structures of their pure component molecules (Table 3). In contrast ϕ for high-spin **1c**, and for all of the low-spin crystals, are essentially equal to the expected values.

The plasticity of the coordination sphere in $[M'(bpp)_2]^{2+}$ should vary according to the d-electron configuration of M′, as M′ = Fe{HS} > Zn > Ni > Fe{LS} ≈ Ru.[80] Hence, this variation in ϕ implies the molecular geometry of high-spin $[Fe(bpp)_2]^{2+}$ in **2c** and **3c** may be influenced by the presence of more rigid dopant molecules. That in turn correlates with the observed structural differences between **1c–3c** during SCO, which appear to reflect the influence of ϕ on their crystal packing rather than the size of the dopant ions (Fig. 8).

$T_{\frac{1}{2}}$ in salts of $[Fe(bpp)_2]^{2+}$ derivatives with terpyridine embrace crystal packing correlates linearly with the change in Θ during SCO ($\Delta\Theta_{SCO}$, Fig. 9).[92,93] Θ is a torsion angle parameter, defined in the ESI,† which reflects the position of the metal coordination geometry along the $O_h \rightarrow D_{3h}$ distortion pathway.[91] While Θ is a function of the whole metal coordination sphere, ϕ and Θ are approximately proportional to each other when other metric parameters are unchanged.[78]

Data in Fig. 9 are plotted as ΔT(latt), which is the lattice contribution to $T_{\frac{1}{2}}$ separated from the molecular ligand field component, which is estimated from solution measurements (eqn (7)).[93,94]

$$\Delta T(\text{latt}) = T_{\frac{1}{2}}(\text{solid}) - T_{\frac{1}{2}}(\text{solution}) \quad (7)$$

The slope of Fig. 9 describes the coupling between the molecular geometry rearrangement and the lattice energy change during SCO in terpyridine embrace crystals.[95]

The average $\Delta\Theta_{SCO}$ for the mixed-metal sites in **1c–3c** (Tables S2–S4, ESI†) bears no relation to the correlation in Fig. 9. However, Θ_{SCO} for their iron centres can be extracted

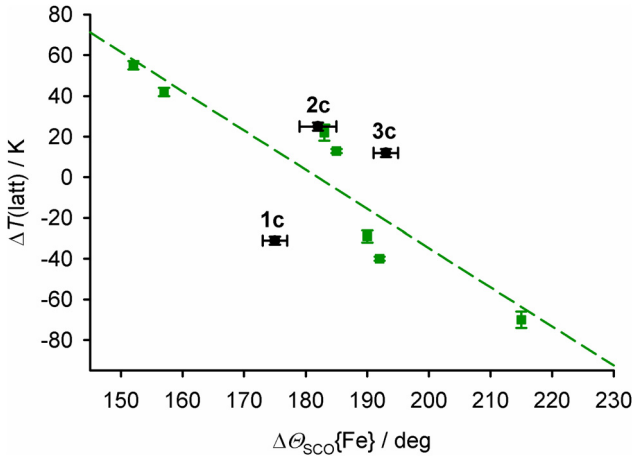

Fig. 9 The relationship between $\Delta\Theta_{SCO}\{Fe\}$ and the lattice contribution to $T_{\frac{1}{2}}$, $\Delta T(latt)$,[93] for salts of $[Fe(bpp)_2]^{2+}$ derivatives with terpyridine embrace crystal packing. The green data points and line show the published correlation,[92] while **1c–3c** are plotted in black.[94]

from these averaged values, by correction for Θ of the dopant molecule (eqn (8), *cf.* eqn (4)).

$$\Theta_{obs} = z\Theta\{Fe\} + (1 - z)\Theta\{M\} \quad (8)$$

The corrected values $\Delta\Theta_{SCO}\{Fe\}$ are shown in Fig. 9. **1c** lies significantly below the correlation line for undoped materials, implying its $\Delta T(latt)$ (and $T_{\frac{1}{2}}$) are lower than predicted from the structural properties of its iron centres. That is, the lattice in **1c** stabilises its high-spin state more efficiently than in the pure iron complex. In contrast, **2c** and **3c** are both a similar distance above the main correlation. That suggests their $\Delta T(latt)$ and $T_{\frac{1}{2}}$ are slightly higher than expected on structural grounds, and to a similar degree. Hence, the doped lattices in **2c** and **3c** influence $T_{\frac{1}{2}}$ to a similar degree, but differently from **1c**.

Lastly, since **2c** and **3c** both lie a similar distance above the main correlation line in Fig. 9, we conclude the higher $T_{\frac{1}{2}}$ in **2c** compared to **3c** is also a function of $\Delta\Theta_{SCO}$; that is, how their iron coordination geometries are modified by the presence of ruthenium(II) and nickel(II) dopants.

Conclusions

The effect of dopant ions 'M' on SCO in $[Fe_zM_{1-z}(bpp)_2][BF_4]_2$ is more complicated than expected, based on previous work.[32–34] Most unexpectedly, $T_{\frac{1}{2}}$ increases with increased ruthenium doping in $[Fe_zRu_{1-z}(bpp)_2][BF_4]_2$ (**2a–2d**; Table 1). That cannot be explained from the ionic radius of Ru^{2+}, which is too large to stabilise the low-spin state of the iron lattice. Rather, it reflects that different dopant ions cause opposite perturbations to the energetics of SCO in the host lattice (Fig. 4). Since another ruthenium-doped SCO crystal also exhibits a higher $T_{\frac{1}{2}}$ than the parent iron complex,[57] that might be a general observation.

Crystallographic analysis of $[Fe_zM_{1-z}(bpp)_2][BF_4]_2$ ($z \approx 0.5$) with M = Zn, Ru and Ni correlates these macroscopic observations with their structures at the molecular level. Small but consistent trends in their molecular structures, unit cell parameters and thermal expansion coefficients imply the influence of zinc dopants on the materials' structures differs from doping with nickel or ruthenium. That is clearly expressed in the structure:function correlation in Fig. 9. This shows **2c** and **3c** behave broadly consistently with each other, with their doped lattices stabilizing the low-spin state of the material compared to the undoped material. However **1c** behaves differently, in that its zinc-doped lattice strongly stabilises the high-spin state. The structure:function properties of the two types of doped material must be considered separately.

We conclude that large dopant ions like zinc(II) in **1c** indeed lower $T_{\frac{1}{2}}$ as previously understood, which is reflected in its smaller ΔV_{SCO} unit cell volume change (Fig. 7).[32–34] However Fig. 8 implies the more distorted coordination geometry of the zinc(II) dopant complex, and its impact on the structure of the iron sites in the material, contributes to ΔV_{SCO} as much as the ionic radius of the zinc(II) ion. In contrast the ruthenium(II) and nickel(II) dopants in **2c** and **3c** exert more moderate, and very similar, chemical pressure on the $[Fe(bpp)_2][BF_4]_2$ lattice (Fig. 9). In that case, the variation of $T_{\frac{1}{2}}$ with composition reflects the different influences of those two dopant ions on the molecular structure of the iron switching centres, and how that feeds through to the bulk lattice (Fig. 8 and 9).

The above implies that salts of $[Fe(bpp)_2]^{2+}$ derivatives with more distorted high-spin molecular geometries and a larger structure change during SCO, should be affected more strongly by ruthenium doping.[96–99] Other moderately sized dopant ions whose coordination geometries impose a regular O_h symmetry preferred by low-spin iron(II) centres, should also increase $T_{\frac{1}{2}}$ most effectively in doped $[Fe_zM_{1-z}L_n]$ lattices. Current work aims to test those predictions, and to probe the generality of our conclusions.

Finally, "molecular alloying"[100] by chemical doping of different metals, ligands and/or anions into SCO materials has been used to tune $T_{\frac{1}{2}}$ towards room temperature for application purposes.[45,100–106] Up to now, metal doping has only been used in such materials undergoing high temperature SCO, to lower their $T_{\frac{1}{2}}$ towards 300 K.[102,103] This study shows how metal doping can increase $T_{\frac{1}{2}}$ towards a desired range, as well as decreasing it. That could have value for adjusting solid-state refrigerants based on SCO materials, for example, to optimise their performance at room temperature.[16–19] While chemical doping also quenches thermal hysteresis in cooperative SCO materials, that is beneficial for cooling applications requiring a first-order transition that is thermodynamically reversible (*ie* with no thermal hysteresis).[107]

Experimental

The precursor complexes $[M'(bpp)_2][BF_4]_2$ (M′ = Fe,[64] Ni,[79] Zn[66] and Ru[67]), and $[Fe_{0.5}Ni_{0.5}(bpp)_2][BF_4]_2$ (**3c**),[54] were prepared by the literature methods.

Synthesis of $[Fe_zZn_{1-z}(bpp)_2][BF_4]_2$ (1a–1e)

Preformed $[Fe(bpp)_2][BF_4]_2$ and $[Zn(bpp)_2][BF_4]_2$ were mixed in different mole ratios, to a combined mass of 0.25 g. The

combined solids were stirred in nitromethane (25 cm^3), until all the solid had dissolved. The solutions were concentrated to *ca.* 10 cm^3, then filtered. Slow diffusion of diethyl ether vapour into the solutions afforded yellow polycrystalline materials, whose colour becomes paler as z decreases. Crystallised yields were in the range 80–85%. The compositions and analytical data for **1a–1e** are given in Table 1.

Synthesis of $[Fe_zRu_{1-z}(bpp)_2][BF_4]_2$ (2a–2d)

Method as above, using $[Ru(bpp)_2][BF_4]_2$ (Table 1). Polycrystalline **2a–2d** are brown in colour, which becomes darker with increased Ru content.

Single crystal structure analyses

Single crystals of **1c**, **2c**, **3c** and the precursor complexes were grown by vapour diffusion methods as described above. Full datasets of the doped crystals were collected at station I19 of the Diamond synchrotron (λ = 0.6889 Å), while variable temperature unit cell data were measured with an Agilent SuperNova diffractometer using Mo-K_α radiation (λ = 0.7107 Å).

Experimental details and refinement protocols for the full structure determinations are given in the ESI.† The structures were solved by direct methods *(SHELX-TL*[108]), and developed by full least-squares refinement on F^2 (*SHELXL2018*[109]). Crystallographic figures were produced using *XSEED*,[110] and other publication materials were prepared with *OLEX*2.[111]

Isotropic and anisotropic thermal expansion parameters at 100 K were calculated with *PASCal*.[90] Thermal expansion coefficients at 300 K were derived from linear regression analyses of unit cell data (eqn (1)). Estimated errors on α_V{300 K} are also based on the *PASCal* calculations.

Other measurements

All physical characterisation was performed using the same sample of each material. CHN elemental microanalyses were performed by the microanalytical service at the London Metropolitan University School of Human Sciences. Energy Dispersive X-Ray (EDX) analysis was carried out using a Jeol JSM-7610F field emission scanning electron microscope with a 15 kV applied voltage; or, with a FEI Nova NanoSEM 450 environmental microscope operating at 3 kV. X-ray powder diffraction data were obtained with a Bruker D8 Advance A25 diffractometer using Cu-K_α radiation (λ = 1.5418 Å). Differential scanning calorimetry (DSC) measurements used a TA Instruments DSC Q20 calorimeter, with heating at a rate of 10 K min^{-1}.

Magnetic susceptibility measurements were performed on a Quantum Design MPMS-2 SQUID or a MPMS-3 SQUID/VSM magnetometer, with an applied field of 5000 G and a scan rate of 2 K min^{-1}. A diamagnetic correction for the samples was estimated from Pascal's constants;[112] a diamagnetic correction for the sample holder was also applied. Processing of magnetic data and all graph plotting was performed using using *SIGMAPLOT*.[113]

Author contributions

The project was conceived and supervised by PC and MAH. PG undertook the synthesis and analytical characterisation of the new materials. HBV and NY measured the magnetic susceptibility data, using SQUID magnetometer time provided by OC and TK. CMP collected the crystallographic data, and MAH did the structure refinements and analysis. CE performed the mechanoelastic model simulations and analysed the results. MAH and CE wrote the manuscript draft, which was reviewed and edited by PC. All authors approved the final version of the publication.

Conflicts of interest

There are no conflicts to declare.

Acknowledgements

The authors thank Dr Alexander Kulak and Dr Namrah Shahid (University of Leeds) for help with some measurements. PC and MAH's collaboration was funded by the Royal Society, UK (IES\R3\193172). PG gratefully acknowledges financial support by the SERB, India (PDF/2021/004430); PC by the SERB (ECR/2018/000923); and CE by the UEFISCDI, Romania (PN-III-P4-ID-PCE-2020-1946). MAH acknowledges Diamond Light Source for access to beamline I19 (CY26879), which contributed to the results presented here.

Notes and references

1 in *Spin Crossover in Transition Metal Compounds I–III: Topics in Current Chemistry*, ed. P. Gütlich and H. A. Goodwin, Springer-Verlag, Berlin, 2004, vols. 233–235.
2 in *Spin-crossover materials – properties and applications*, ed. M. A. Halcrow, John Wiley & Sons, Chichester, UK, 2013, p. 568.
3 J. Zarembowitch, F. Varret, A. Hauser, J. A. Real and K. Boukheddaden, *C. R. Chim*, 2018, **21**, 1056–1059.
4 K. Senthil Kumar and M. Ruben, *Coord. Chem. Rev.*, 2017, **346**, 176–205.
5 G. Molnár, S. Rat, L. Salmon, W. Nicolazzi and A. Bousseksou, *Adv. Mater.*, 2018, **30**, 1703862.
6 O. Kahn, J. Kröber and C. Jay, *Adv. Mater.*, 1992, **4**, 718–728.
7 M. D. Manrique-Juárez, S. Rat, L. Salmon, G. Molnár, C. M. Quintero, L. Nicu, H. J. Shepherd and A. Bousseksou, *Coord. Chem. Rev.*, 2016, **308**, 395–408.
8 M. Wang, Z.-Y. Li, R. Ishikawa and M. Yamashita, *Coord. Chem. Rev.*, 2021, **435**, 213819.
9 Y. Sekine, R. Akiyoshi and S. Hayami, *Coord. Chem. Rev.*, 2022, **469**, 214663.
10 A. B. Gaspar and M. Seredyuk, *Coord. Chem. Rev.*, 2014, **268**, 41–58.
11 A. Enriquez-Cabrera, A. Rapakousiou, M. Piedrahita Bello, G. Molnár, L. Salmon and A. Bousseksou, *Coord. Chem. Rev.*, 2020, **419**, 213396.

12 M. K. Javed, A. Sulaiman, M. Yamashita and Z.-Y. Li, *Coord. Chem. Rev.*, 2022, **467**, 214625; K. Sun, J.-P. Xue, Z.-S. Yao and J. Tao, *Dalton Trans.*, 2022, **51**, 16044–16054.
13 E. Coronado, *Nat. Rev. Mater.*, 2020, **5**, 87–104.
14 K. Senthil Kumar and M. Ruben, *Angew. Chem., Int. Ed.*, 2021, **60**, 7502–7521.
15 L. Kipgen, M. Bernien, F. Tuczek and W. Kuch, *Adv. Mater.*, 2021, **33**, 2008141 and 2021, **33**, 2170354 (correction).
16 S. P. Vallone, A. N. Tantillo, A. M. dos Santos, J. Molaison, R. Kulmaczewski, A. Chapoy, P. Ahmadi, M. A. Halcrow and K. G. Sandeman, *Adv. Mater.*, 2019, **31**, 1807334.
17 K. Ridier, Y. Zhang, M. Piedrahita-Bello, C. M. Quintero, L. Salmon, G. Molnár, C. Bergaud and A. Bousseksou, *Adv. Mater.*, 2020, **32**, 2000987.
18 M. Romanini, Y. Wang, K. Gürpinar, G. Ornelas, P. Lloveras, Y. Zhang, W. Zheng, M. Barrio, A. Aznar, A. Gràcia-Condal, B. Emre, O. Atakol, C. Popescu, H. Zhang, Y. Long, L. Balicas, J. L. Tamarit, A. Planes, M. Shatruk and L. Mañosa, *Adv. Mater.*, 2021, **33**, 2008076.
19 J. Seo, J. D. Braun, V. M. Dev and J. A. Mason, *J. Am. Chem. Soc.*, 2022, **144**, 6493–6503.
20 M. D. Manrique-Juárez, F. Mathieu, V. Shalabaeva, J. Cacheux, S. Rat, L. Nicu, T. Leïchlé, L. Salmon, G. Molnár and A. Bousseksou, *Angew. Chem., Int. Ed.*, 2017, **56**, 8074–8078.
21 M. D. Manrique-Juárez, F. Mathieu, A. Laborde, S. Rat, V. Shalabaeva, P. Demont, O. Thomas, L. Salmon, T. Leïchlé, L. Nicu, G. Molnár and A. Bousseksou, *Adv. Funct. Mater.*, 2018, **28**, 1801970.
22 M. Piedrahita-Bello, J. E. Angulo-Cervera, A. Enriquez-Cabrera, G. Molnár, B. Tondu, L. Salmon and A. Bousseksou, *Mater. Horiz.*, 2021, **8**, 3055–3062.
23 V. Nagy, I. Suleimanov, G. Molnár, L. Salmon, A. Bousseksou and L. Csóka, *J. Mater. Chem. C*, 2015, **3**, 7897–7905.
24 M. Piedrahita-Bello, J. E. Angulo-Cervera, R. Courson, G. Molnár, L. Malaquin, C. Thibault, B. Tondu, L. Salmon and A. Bousseksou, *J. Mater. Chem. C*, 2020, **8**, 6001–6005.
25 O. I. Kucheriv, V. V. Oliynyk, V. V. Zagorodnii, V. L. Launets and I. A. Gural'skiy, *Sci. Rep.*, 2016, **6**, 38334.
26 A. Tsukiashi, K. S. Min, H. Kitayama, H. Terasawa, S. Yoshinaga, M. Takeda, L. F. Lindoy and S. Hayami, *Sci. Rep.*, 2018, **8**, 14911.
27 O. Calvez, H. Camon, K. Ridier, G. Molnár and O. Gauthier-Lafaye, *Appl. Opt.*, 2022, **61**, 9562–9568.
28 E. Resines-Urien, E. Fernandez-Bartolome, A. Martinez-Martinez, A. Gamonal, L. Piñeiro-López and J. S. Costa, *Chem. Soc. Rev.*, 2023, **52**, 705–727.
29 M. Chergui and E. Collet, *Chem. Rev.*, 2017, **117**, 11025–11065.
30 K. J. Gaffney, *Chem. Sci.*, 2021, **12**, 8010–8025.
31 P. Guionneau, M. Marchivie and G. Chastanet, *Chem. – Eur. J.*, 2021, **27**, 1483–1486.
32 P. Gütlich, A. Hauser and H. Spiering, *Angew. Chem., Int. Ed.*, 1994, **33**, 2024–2054.
33 A. Hauser, J. Jeftić, H. Romstedt, R. Hinek and H. Spiering, *Coord. Chem. Rev.*, 1999, **190–192**, 471–491.
34 A.-I. Popa, L. Stoleriu and C. Enachescu, *J. Appl. Phys.*, 2021, **129**, 131101.
35 G. Chastanet, C. Desplanches, C. Baldé, P. Rosa, M. Marchivie and P. Guionneau, *Chem. Sq.*, 2018, **2**, 2.
36 X. Li, D. Zhang, Y. Qian, W. Liu, C. Mathonière, R. Clérac and X. Bao, *J. Am. Chem. Soc.*, 2023, **145**, 9564–9570.
37 J.-P. Martin, J. Zarembowitch, A. Bousseksou, A. Dworkin, J. G. Haasnoot and F. Varret, *Inorg. Chem.*, 1994, **33**, 6325–6333.
38 N. Paradis, G. Chastanet, T. Palamarciuc, P. Rosa, F. Varret, K. Boukheddaden and J.-F. Letard, *J. Phys. Chem. C*, 2015, **119**, 20039–20050.
39 N. Paradis, G. Chastanet, F. Varret and J.-F. Letard, *Eur. J. Inorg. Chem.*, 2013, 968–974.
40 C. Baldé, C. Desplanches, F. Le Gac, P. Guionneau and J.-F. Létard, *Dalton Trans.*, 2014, **43**, 7820–7829.
41 H. Wang, C. Baldé, A. Grosjean, C. Desplanches, P. Guionneau and G. Chastanet, *Dalton Trans.*, 2018, **47**, 14741–14750.
42 M. A. Halcrow and G. Chastanet, *Polyhedron*, 2017, **136**, 5–12.
43 C. Balde, C. Desplanches, M. Grunert, Y. Wei, P. Gütlich and J.-F. Létard, *Eur. J. Inorg. Chem.*, 2008, 5382–5389.
44 C. Baldé, C. Desplanches, A. Wattiaux, P. Guionneau, P. Gütlich and J.-F. Létard, *Dalton Trans.*, 2008, 2702–2707.
45 R. Diego, O. Roubeau and G. Aromí, *Chem Sq.*, 2021, **5**, 1.
46 Z. Yu, T. Kuroda-Sowa, H. Kume, T. Okubo, M. Maekawa and M. Munakata, *Bull. Chem. Soc. Jpn.*, 2009, **82**, 333–337.
47 A. Rotaru, M. M. Dîrtu, C. Enachescu, R. Tanasa, J. Linares, A. Stancu and Y. Garcia, *Polyhedron*, 2009, **28**, 2531–2536.
48 M. S. Sylla, C. Baldé, N. Daro, C. Desplanches, M. Marchivie and G. Chastanet, *Eur. J. Inorg. Chem.*, 2018, 297–304.
49 C. Das, S. Dey, A. Adak, C. Enachescu and P. Chakraborty, *Cryst. Growth Des.*, 2023, **23**, 3496–3508.
50 T. Tayagaki, A. Galet, G. Molnár, M. C. Muñoz, A. Zwick, K. Tanaka, J. A. Real and A. Bousseksou, *J. Phys. Chem. B*, 2005, **109**, 14859–14867.
51 Y. Avila, R. Terrero, P. M. Crespo, L. A. Díaz-Paneque, M. González, M. Ávila and E. Reguera, *Eur. J. Inorg. Chem.*, 2021, 3969–3980.
52 J.-P. Martin, J. Zarembowitch, A. Dworkin, J. G. Haasnoot and E. Codjovi, *Inorg. Chem.*, 1994, **33**, 2617–2623.
53 C. Baldé, C. Desplanches, J.-F. Létard and G. Chastanet, *Polyhedron*, 2017, **123**, 138–144.
54 C. A. Tovee, C. A. Kilner, J. A. Thomas and M. A. Halcrow, *CrystEngComm*, 2009, **11**, 2069–2077. $[Fe_{0.5}Ni_{0.5}(bpp)_2][BF_4]_2$ from this paper is reexamined in this study, as compound **3c**.
55 R. D. Shannon, *Acta Crystallogr., Sect. A: Cryst. Phys., Diffr., Theor. Gen. Crystallogr.*, 1976, **32**, 751–767.
56 Low-spin states of metal complexes have been stabilised by including them in the pores of a framework lattice. The restricted pore volume of the rigid host framework exerts a localised mechanical pressure on the guest complex molecules. A. Hauser, N. Amstutz, S. Delahaye, A. Sadki, S. Schenker, R. Sieber and M. Zerara, *Struct. Bonding*, 2004, **106**, 81–96.
57 P. Chakraborty, M. Sy, H. Fourati, T. Delgado, M. Dutta, C. Das, C. Besnard, A. Hauser, C. Enachescu and K. Boukheddaden, *Phys. Chem. Chem. Phys.*, 2022, **24**, 982–994.

58 E. W. Müller, J. Ensling, H. Spiering and P. Gütlich, *Inorg. Chem.*, 1983, **22**, 2074–2078.
59 S. Lakhloufi, P. Guionneau, M. H. Lemée-Cailleau, P. Rosa and J.-F. Létard, *Phys. Rev. B*, 2010, **82**, 132104.
60 J. Kusz, M. Zubko, R. B. Neder and P. Gütlich, *Acta Crystallogr., Sect. B: Struct. Sci.*, 2012, **68**, 40–56.
61 E. Collet, G. Azzolina, J. Jeftić and M.-H. Lemée-Cailleau, *Adv. Phys.: X*, 2023, **8**, 2161936.
62 F. J. Valverde-Muñoz, R. G. Torres Ramírez, A. Ulhe, E. Trzop, M. Dutta, C. Das, P. Chakraborty and E. Collet, *CrystEngComm*, 2023, **25**, 3588–3597.
63 J. Jeftić and A. Hauser, *J. Phys. Chem. B*, 1997, **101**, 10262–10270.
64 J. M. Holland, J. A. McAllister, Z. Lu, C. A. Kilner, M. Thornton-Pett and M. A. Halcrow, *Chem. Commun.*, 2001, 577–578.
65 We have investigated doping $[Ru(terpy)_2]^{2+}$ (terpy = 2,2′:6′,2″-terpyridine) and related molecules into the $[Fe(bpp)_2][BF_4]_2$ lattice, as a potential route to emissive SCO materials. There is a more complicated relationship between composition and $T_{\frac{1}{2}}$ in solid solutions of two non-isomorphous molecules. See ref. 54, and L. J. Kershaw Cook and M. A. Halcrow, *Polyhedron*, 2015, **87**, 91–97.
66 N. K. Solanki, M. A. Leech, E. J. L. McInnes, F. E. Mabbs, J. A. K. Howard, C. A. Kilner, J. M. Rawson and M. A. Halcrow, *J. Chem. Soc., Dalton Trans.*, 2002, 1295–1301.
67 M. A. Halcrow, *Chem. Commun.*, 2010, **46**, 4761–4763.
68 $[Fe(bpp)_2][BF_4]_2$ is yellow in its high-spin state, and dark brown when low-spin (ref. 64). For comparison, pure $[Zn(bpp)_2][BF_4]_2$ is colourless; $[Ru(bpp)_2][BF_4]_2$ is yellow as a powder but forms orange single crystals; and $[Ni(bpp)_2][BF_4]_2$ is blue.
69 L. Stoleriu, M. Nishino, S. Miyashita, A. Stancu and C. Enachescu, *Phys. Rev. B*, 2017, **96**, 064115.
70 N. di Scala, N. E. Belmouri, M. A. P. Espejo and K. Boukheddaden, *Phys. Rev. B*, 2022, **106**, 014422.
71 T. Delgado, C. Enachescu, A. Tissot, L. Guénée, A. Hauser and C. Besnard, *Phys. Chem. Chem. Phys.*, 2018, **20**, 12493–12502.
72 L. Stoleriu, P. Chakraborty, A. Hauser, A. Stancu and C. Enachescu, *Phys. Rev. B*, 2011, **84**, 134102.
73 C. Enachescu and A. Hauser, *Phys. Chem. Chem. Phys.*, 2016, **18**, 20591–20599.
74 H. Hsu, C. P. Crisostomo, W. Wang and Z. Wu, *Phys. Rev. B*, 2021, **103**, 054401.
75 A. Railean, M. Kelai, A. Bellec, V. Repain, M. L. Boillot, T. Mallah, L. Stoleriu and C. Enachescu, *Phys. Rev. B*, 2023, **107**, 014304.
76 J. Kusz, H. Spiering and P. Gütlich, *J. Appl. Crystallogr.*, 2004, **37**, 589–595 (ref. 114).
77 Some metal ratios used in the mechanoelastic simulations in Fig. 4 are slightly different from the sample compositions z in Table 1. That is because the simulations were done before we had completed the analytical characterisation of the materials. However the differences are within the experimental error on z, and do not affect the conclusions of our study.
78 L. J. Kershaw Cook, R. Mohammed, G. Sherborne, T. D. Roberts, S. Alvarez and M. A. Halcrow, *Coord. Chem. Rev.*, 2015, **289–290**, 2–12.
79 J. M. Holland, C. A. Kilner, M. Thornton-Pett and M. A. Halcrow, *Polyhedron*, 2001, **20**, 2829–2840.
80 S. Alvarez, *Chem. Rev.*, 2015, **115**, 13447–13483.
81 S. Vela, J. J. Novoa and J. Ribas-Arino, *Phys. Chem. Chem. Phys.*, 2014, **16**, 27012–27024. This is a computational study comparing SCO in $[Fe(bpp)_2][BF_4]_2$ and $[Fe(bpp)_2][PF_6]_2$. The high-spin PF_6^- salt crystallises in a highly distorted geometry with $\phi = 154^\circ$, and two bpp ligands canted 28° away from the perpendicular. That distorted high-spin geometry perturbs the ligand field at the iron atom, which was calculated to lower the thermodynamic $T_{\frac{1}{2}}$ of $[Fe(bpp)_2][PF_6]_2$ by 13 K. Hence, the much smaller changes to ϕ induced by the dopants in **2c**–**3c** should contribute no more than 1–2 K to the higher $T_{\frac{1}{2}}$ in **2c**, at the molecular level.
82 R. Pritchard, C. A. Kilner and M. A. Halcrow, *Chem. Commun.*, 2007, 577–579.
83 I. Dance and M. Scudder, *CrystEngComm*, 2009, **11**, 2233–2247.
84 A. van der Lee and D. G. Dumitrescu, *Chem. Sci.*, 2021, **12**, 8537–8547.
85 A. D. Bond, *Acta Crystallogr., Sect. B: Struct. Crystallogr. Cryst. Chem.*, 2021, **77**, 357–364.
86 V. A. Money, I. R. Evans, M. A. Halcrow, A. E. Goeta and J. A. K. Howard, *Chem. Commun.*, 2003, 158–159.
87 L. Wiehl, G. Kiel, C. P. Köhler, H. Spiering and P. Gütlich, *Inorg. Chem.*, 1986, **25**, 1565–1571 (ref. 114).
88 J. Kusz, H. Spiering and P. Gütlich, *J. Appl. Cryst.*, 2001, **34**, 229–238 (ref. 114).
89 P. Guionneau, M. Marchivie, G. Bravic, J.-F. Létard and D. Chasseau, *J. Mater. Chem.*, 2002, **12**, 2546–2551.
90 M. J. Cliffe and A. L. Goodwin, *J. Appl. Cryst.*, 2012, **45**, 1321–1329.
91 P. Guionneau, M. Marchivie, G. Bravic, J.-F. Létard and D. Chasseau, *Top. Curr. Chem.*, 2004, **234**, 97–128.
92 E. Michaels, C. M. Pask, I. Capel Berdiell, H. B. Vasili, M. J. Howard, O. Cespedes and M. A. Halcrow, *Cryst. Growth Des.*, 2022, **22**, 6809–6817.
93 M. A. Halcrow, I. Capel Berdiell, C. M. Pask and R. Kulmaczewski, *Inorg. Chem.*, 2019, **58**, 9811–9821.
94 $[Fe(bpp)_2][BF_4]_2$ exhibits $T_{\frac{1}{2}} = 248$ K in solution, so $\Delta T(\text{latt}) = T_{\frac{1}{2}} - 248$ for **1c**–**3c** (ref. 93).
95 A multivariate structure:function analysis of SCO in salts of $[Fe(bpp)_2]^{2+}$ derivatives was published while this article was under review. L. Marchi, S. Fantuzzi, A. Cingolani, A. Messori, R. Mazzoni, S. Zacchini, M. Cocchi and L. Rigamonti, *Dalton Trans.*, 2023, **52**, 7684–7694.
96 L. J. Kershaw Cook, F. L. Thorp-Greenwood, T. P. Comyn, O. Cespedes, G. Chastanet and M. A. Halcrow, *Inorg. Chem.*, 2015, **54**, 6319–6330.
97 I. Capel Berdiell, R. Kulmaczewski, N. Shahid, O. Cespedes and M. A. Halcrow, *Chem. Commun.*, 2021, **57**, 6566–6569.

98 N. Suryadevara, A. Mizuno, L. Spieker, S. Salamon, S. Sleziona, A. Maas, E. Pollmann, B. Heinrich, M. Schleberger, H. Wende, S. K. Kuppusamy and M. Ruben, *Chem. – Eur. J.*, 2022, **28**, e202103853.
99 R. Kulmaczewski, L. J. Kershaw Cook, C. M. Pask, O. Cespedes and M. A. Halcrow, *Cryst. Growth Des.*, 2022, **22**, 1960–1971.
100 O. Kahn, L. Sommier and E. Codjovi, *Chem. Mater.*, 1997, **9**, 3199–3205.
101 J. Kröber, E. Codjovi, O. Kahn, F. Grolière and C. Jay, *J. Am. Chem. Soc.*, 1993, **115**, 9810–9811.
102 J. R. Galán-Mascarós, E. Coronado, A. Forment-Aliaga, M. Monrabal-Capilla, E. Pinilla-Cienfuegos and M. Ceolin, *Inorg. Chem.*, 2010, **49**, 5706–5714.
103 C. Lefter, S. Tricard, H. Peng, G. Molnár, L. Salmon, P. Demont, A. Rotaru and A. Bousseksou, *J. Phys. Chem. C*, 2015, **119**, 8522–8529.
104 M. Piedrahita-Bello, B. Martin, L. Salmon, G. Molnár, P. Demont and A. Bousseksou, *J. Mater. Chem. C*, 2020, **8**, 6042–6051.
105 C. Bartual-Murgui, C. Perez-Padilla, S. J. Teat, O. Roubeau and G. Aromí, *Inorg. Chem.*, 2020, **59**, 12132–12142.
106 Y. Gong, Z.-H. Li, X. Yan, Y.-Q. Wang, C.-Y. Zhao, W.-K. Han, Q.-T. Hu, H.-S. Lu and Z.-G. Gu, *Chem. – Eur. J.*, 2020, **26**, 12472–12480.
107 K. G. Sandeman, *APL Mater.*, 2016, **4**, 111102.
108 G. M. Sheldrick, *Acta Crystallogr., Sect. A: Found. Crystallogr.*, 2015, **71**, 3–8.
109 G. M. Sheldrick, *Acta Crystallogr., Sect. B: Struct. Sci.*, 2015, **71**, 3–8.
110 L. J. Barbour, *J. Appl. Cryst.*, 2020, **53**, 1141–1146.
111 O. V. Dolomanov, L. J. Bourhis, R. J. Gildea, J. A. K. Howard and H. Puschmann, *J. Appl. Cryst.*, 2009, **42**, 339–341.
112 C. J. O'Connor, *Prog. Inorg. Chem.*, 1982, **29**, 203–283.
113 *SIGMAPLOT, version 8.02*, SPSS Inc., 2002.
114 Ref. 76, 87 and 88 describe a theoretical treatment of thermal expansion in SCO crystals, based on the theory of elastic lattice interactions. The α coefficient derived in these studies is not the same as the widely used α_V thermal expansion parameter in eqn (5) (ref. 84, 85 and 90).

